Search for double-β decay of ^{76}Ge to excited states of ^{76}Se with the MAJORANA DEMONSTRATOR

I. J. Arnquist,[1] F. T. Avignone III,[2,3] A. S. Barabash,[4] C. J. Barton,[5] F. E. Bertrand,[3] E. Blalock,[6,7] B. Bos,[8,7] M. Busch,[9,7]
M. Buuck,[10] T. S. Caldwell,[8,7] Y-D. Chan,[11] C. D. Christofferson,[12] P.-H. Chu,[13] M. L. Clark,[8,7] C. Cuesta,[14] J. A. Detwiler,[10]
A. Drobizhev,[11] T. R. Edwards,[13,5] D. W. Edwins,[2] Yu. Efremenko,[15,3] H. Ejiri,[16] S. R. Elliott,[13] T. Gilliss,[8,7]
G. K. Giovanetti,[17] M. P. Green,[6,7,3] J. Gruszko,[8,7] I. S. Guinn ⦿,[8,7] V. E. Guiseppe,[3] C. R. Haufe,[8,7] R. Henning,[8,7]
D. Hervas Aguilar,[8,7] E. W. Hoppe,[1] A. Hostiuc,[10] M. F. Kidd,[18] I. Kim,[13] R. T. Kouzes,[1] A. M. Lopez,[15]
J. M. López-Castaño,[5] E. L. Martin,[8,7] R. D. Martin,[19] R. Massarczyk,[13] S. J. Meijer,[13] S. Mertens,[20,21] J. Myslik,[11] T. K. Oli,[5]
G. Othman,[8,7] L. S. Paudel,[5] W. Pettus,[10] A. W. P. Poon,[11] D. C. Radford,[3] A. L. Reine,[8,7] K. Rielage,[13] N. W. Ruof,[10]
B. Saykı,[13] M. J. Stortini,[13] D. Tedeschi,[2] R. L. Varner,[3] S. Vasilyev,[22] J. F. Wilkerson,[8,7,3] C. Wiseman,[10] W. Xu,[5] C.-H. Yu,[3]
and B. X. Zhu[13,*]

(MAJORANA Collaboration)

[1]*Pacific Northwest National Laboratory, Richland, Washington 99354, USA*
[2]*Department of Physics and Astronomy, University of South Carolina, Columbia, South Carolina 29208, USA*
[3]*Oak Ridge National Laboratory, Oak Ridge, Tennessee 37830, USA*
[4]*National Research Center "Kurchatov Institute" Institute for Theoretical and Experimental Physics, Moscow 117218, Russia*
[5]*Department of Physics, University of South Dakota, Vermillion, South Dakota 57069, USA*
[6]*Department of Physics, North Carolina State University, Raleigh, North Carolina 27695, USA*
[7]*Triangle Universities Nuclear Laboratory, Durham, North Carolina 27708, USA*
[8]*Department of Physics and Astronomy, University of North Carolina, Chapel Hill, North Carolina 27514, USA*
[9]*Department of Physics, Duke University, Durham, North Carolina 27708, USA*
[10]*Center for Experimental Nuclear Physics and Astrophysics, and Department of Physics, University of Washington,
Seattle, Washington 98195, USA*
[11]*Nuclear Science Division, Lawrence Berkeley National Laboratory, Berkeley, California 94720, USA*
[12]*South Dakota School of Mines and Technology, Rapid City, South Dakota 57701, USA*
[13]*Los Alamos National Laboratory, Los Alamos, New Mexico 87545, USA*
[14]*Centro de Investigaciones Energéticas, Medioambientales y Tecnológicas, CIEMAT, 28040 Madrid, Spain*
[15]*Department of Physics and Astronomy, University of Tennessee, Knoxville, Tennessee 37916, USA*
[16]*Research Center for Nuclear Physics, Osaka University, Ibaraki, Osaka 567-0047, Japan*
[17]*Physics Department, Williams College, Williamstown, Massachusetts 01267, USA*
[18]*Tennessee Tech University, Cookeville, Tennessee 38505, USA*
[19]*Department of Physics, Engineering Physics and Astronomy, Queen's University, Kingston, Canada ON K7L 3N6*
[20]*Max-Planck-Institut für Physik, München 80805, Germany*
[21]*Physik Department and Excellence Cluster Universe, Technische Universität, München 85748 Germany*
[22]*Joint Institute for Nuclear Research, Dubna 141980, Russia*

The MAJORANA DEMONSTRATOR is a neutrinoless double-β decay search consisting of a low-background modular array of high-purity germanium detectors, $\sim 2/3$ of which are enriched to 88% in ^{76}Ge. The experiment is also searching for double-beta decay of ^{76}Ge to excited states (e.s.) in ^{76}Se. ^{76}Ge can decay into three daughter states of ^{76}Se, with clear event signatures consisting of a $\beta\beta$-decay followed by the prompt emission of one or two γ rays. This results with high probability in multi-detector coincidences. The granularity of the DEMONSTRATOR detector array enables powerful discrimination of this event signature from backgrounds. Using 41.9 kg yr of isotopic exposure, the DEMONSTRATOR has set world leading limits for each e.s. decay of ^{76}Ge, with 90% CL lower half-life limits in the range of $(0.75$–$4.0) \times 10^{24}$ yr. In particular, for the 2ν transition to the first 0^+ e.s. of ^{76}Se, a lower half-life limit of 7.5×10^{23} yr at 90% CL was achieved.

I. INTRODUCTION

Neutrinoless double-beta decay ($0\nu\beta\beta$) is a hypothetical lepton number violating process that, if discovered, would indicate the existence of physics beyond the standard model

---

*Present address: Jet Propulsion Laboratory, California Institute of Technology, Pasadena, CA 91109, USA.

(BSM) [1–7]. In particular, discovery would indicate that the neutrino is a Majorana fermion (i.e., its own antiparticle) [8,9], and might provide a feasible mechanism for generation of the observed matter-antimatter asymmetry of the universe [10,11]. For a set of BSM physics interactions generating $0\nu\beta\beta$ enumerated i, the half-life of $0\nu\beta\beta$ would follow

$$\left[T_{1/2}^{0\nu}\right]^{-1} = \left| \sum_i G_i^{0\nu} \left|M_i^{0\nu}\right|^2 \eta_i^2 \right|, \qquad (1)$$

where $G_i^{0\nu}$ is the phase-space integral, $M_i^{0\nu}$ is the nuclear matrix element, and η_i represents the amplitude of a general lepton number violating process. The minimal extension to the standard model for providing Majorana neutrino mass adds a heavy right-handed neutrino, and generates a light mass for the standard model neutrino via the type I seesaw mechanism. Under this mechanism, the half-life would follow

$$\left[T_{1/2}^{0\nu}\right]^{-1} = G^{0\nu}\left(g_A^{\text{eff},0\nu}\right)^4 |M^{0\nu}|^2 \langle m_{\beta\beta}\rangle^2, \qquad (2)$$

where $\langle m_{\beta\beta}\rangle$ is the effective Majorana mass of the electron neutrino, and $g_A^{\text{eff},0\nu} = q g_A$ ($g_A = 1.27$) is the axial vector coupling constant, with an empirical quenching term q applied [12]. In this case, a half-life measurement would provide information about the neutrino mass, while the phase-space factor can be precisely calculated [13,14], an $m_{\beta\beta}$ measurement is subject to currently large uncertainties in calculations of $(g_A^{\text{eff},0\nu})^4 |M^{0\nu}|^2$ [15].

Two-neutrino double-beta decay ($2\nu\beta\beta$) is a second-order weak process that has been directly observed in 11 isotopes, with half-lives ranging from 10^{18}–10^{24} yr [16]. The $2\nu\beta\beta$ half-life can be expressed as

$$\left[T_{1/2}^{2\nu}\right]^{-1} = G^{2\nu}\left(g_A^{\text{eff},2\nu}\right)^4 |M^{2\nu}|^2. \qquad (3)$$

Because this formula does not depend on unknown physics factors and the phase-space factor can be accurately calculated, a $2\nu\beta\beta$ half-life measurement allows direct measurement of $(g_A^{\text{eff},2\nu})^4 |M^{2\nu}|^2$. Furthermore, since nuclear matrix elements are calculated using similar techniques for $2\nu\beta\beta$ and $0\nu\beta\beta$ half-lives, such a measurement may help in evaluating $(g_A^{\text{eff},0\nu})^4 |M^{0\nu}|$.

$\beta\beta$ decay, in both 0ν and 2ν modes, can produce daughter nuclei in either the ground state (g.s.) or an excited state (e.s.). Transitions to an e.s. can be distinguished from g.s. transitions by a lower Q value and the prompt emission of one or more γ rays. $\beta\beta$-decay transitions are allowed for transitions from parent 0^+ g.s. to 0^+ and 2^+ states. The half-lives of decays to excited states are heavily suppressed compared to the ground state decay. The primary reason for this is energetic suppression in the phase space due to the reduced Q values for decays to e.s., in addition, decays to 2^+ states experience further suppression due to conservation of angular momentum.

So far, the only $\beta\beta$ to e.s. observations have been $2\nu\beta\beta$ transitions to the first excited 0^+ (0_1^+) daughter states, in two isotopes. In ^{100}Mo, this transition was first measured in 1995 [17], and the global average including additional measurements is $T_{1/2}^{2\nu} = (6.7^{+0.5}_{-0.4}) \times 10^{20}$ yr [16]. In ^{150}Nd, this transition was first measured in 2004 [18,19], and the global average including additional measurements is $T_{1/2}^{2\nu} =$

$(1.2^{+0.3}_{-0.2}) \times 10^{20}$ yr [16]. Searches have been performed in a variety of other isotopes as well [20].

^{76}Ge is a promising isotope for studying $\beta\beta$ decay, with the MAJORANA DEMONSTRATOR [21,22] and GERDA [23,24] experiments currently conducting sensitive searches for $0\nu\beta\beta$, and LEGEND-200 under construction [25]. In addition to the ground state, ^{76}Ge can decay to three excited states of ^{76}Se, as shown in Fig. 1. Experiments have searched for these e.s. decay modes since 1977 [26]; current best limits have been set by GERDA phase I [27]. Among e.s. decay modes, the decay to the 0_1^+ e.s. of ^{76}Se is expected to dominate, with recent half-life predictions falling in the range 1.0×10^{23}–7.1×10^{24} yr [20].

A measurement of the half-life of decay modes to various daughter states provides useful information beyond that provided from just g.s. measurements. As in g.s. measurements, $2\nu\beta\beta$ to e.s. half-lives can be used to obtain direct measurements of $(g_A^{\text{eff},2\nu})^4 |M^{2\nu}|^2$, providing a useful cross-check for the calculation techniques. In addition, a measurement of the nuclear matrix element for $2\nu\beta\beta$ transitions to 2^+ states would enable a sensitive test for a bosonic component to the neutrino wave function [28,29]. An experiment that measured $0\nu\beta\beta$ to both the ground state and 0_1^+ state could use the ratio between these values to test the beyond the standard model physics mechanism generating these processes [30].

II. THE MAJORANA DEMONSTRATOR

The MAJORANA DEMONSTRATOR is studying $\beta\beta$ decay of ^{76}Ge using high-purity germanium (HPGe) detectors. The experiment consists of two modules, each consisting of an array of detectors operated in vacuum in separate cryostats. 58 detectors totalling 44.1 kg are used, 29.7 kg of which are enriched to 88% in ^{76}Ge, allowing them to act as both the source and detector of $\beta\beta$ decay. The remaining detectors have the natural isotopic abundance of 7.8% ^{76}Ge. The HPGe detectors use the P-type point contact (PPC) detector geometry, which has advantages in energy resolution and sensitivity to event topology [31]. The PPC geometry and the granularity of the detector array enable discrimination of single- and multisite events [32].

In order to minimize backgrounds, the experiment is constructed using carefully selected low background materials [33]. The support material and cryostats housing the array primarily consists of underground electroformed copper (UGEFCu). Carefully selected, commercially available materials were selected for the remaining materials, including cabling, cryostat seals, and insulating materials. Low-background front-end electronics were developed for the experiment and are placed next to the detector contacts, enabling low noise measurements [34]. The modules are placed inside of a graded shield, with lower background shield materials used nearer to the detectors. The inner most shield layers consist of 5 cm of UGEFCu followed by 5 cm of commercially available oxygen-free electronic (C10100) copper. The next layer includes 45 cm of lead shielding. These layers are contained in a stainless steel radon exclusion box that is constantly purged with liquid nitrogen boil-off gas. The vacuum hardware, cryogenic hardware, electronics, and
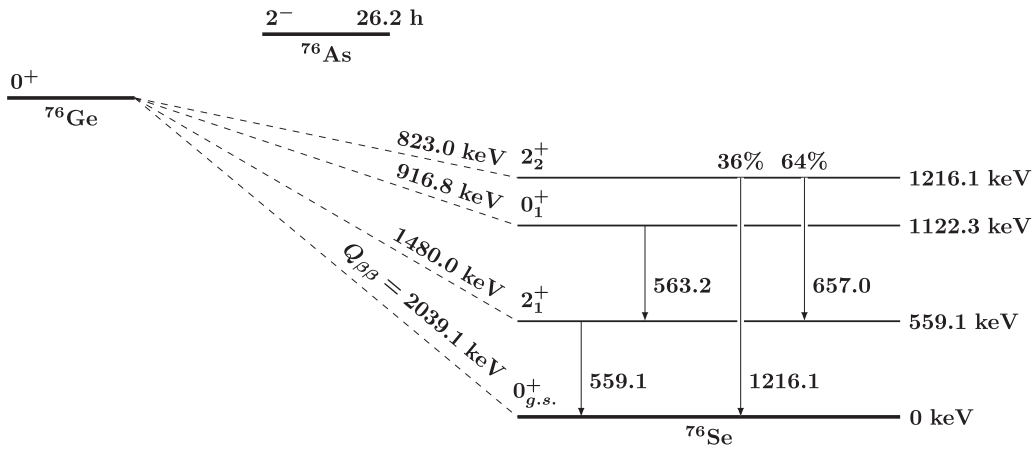
FIG. 1. Level diagram of the $\beta\beta$ decay of ^{76}Ge into ^{76}Se [39].

calibration hardware sit outside of these layers, with a small gap carved out of the lead structure for a cross arm connecting these to the cryostats. Surrounding this is 5 cm of borated polyethylene and 25 cm of unborated polyethylene neutron shielding, and finally scintillating plastic veto panels surround the experiment, used to actively veto backgrounds caused by muons [35]. Each layer of shielding, with inserted cryostats, is shown in Fig. 2. The experiment is housed at the 4850' level (4300 m.w.e) of the Sanford Underground Research Facility (SURF) in order to minimize exposure to cosmic ray muons.

HPGe detector waveforms are recorded by digitizers developed for the GRETINA experiment [36], with a sampling frequency of 100 MHz and 14 bits of resolution [37]. Each detector records on two channels, characterized by gains that differ by a factor of 3; the high gain channel has better signal to noise ratio and is preferred for detector hits with <4 MeV of energy. Each detection channel triggers independently using an internal trapezoidal filter, with an energy threshold typically <1 keV. Upon triggering, either a 20 μs waveform at the full sampling rate, or a 38 μs multisampled waveform with post-rising edge using four presummed samples is read out and stored on disk, to be reanalyzed. Waveforms are corrected

FIG. 2. Diagram of the MAJORANA DEMONSTRATOR showing each shield layer, the inserted cryostats with their detector arrays, and the module hardware outside of the shielding.

for digitizer nonlinearity [38] and energies are calculated using a charge-trapping corrected trapezoidal filter [22]. This procedure produces an energy resolution for all combined detectors of 2.95 keV at full width half-maximum (FWHM) at the ^{208}Th 2614 keV peak, leading the current generation of $\beta\beta$-decay experiments [22].

Module 1 began operation in December 2015, and both DEMONSTRATOR modules have been in nearly continuous operation since August 2016. The set of runs used for this analysis is a subset of those used in Ref. [22], excluding runs recorded before the installation of the inner copper shield. A statistical blinding scheme was applied to much of this data, with cycles of 93 h of blind data and 31 h of open data. Approximately 50% of the isotopic exposure used in this result was in blind runs. The data is divided into eight datasets, labeled DS1, DS2, DS3, DS4, DS5a, DS5b, DS5c, and DS6a. The datasets represent changes in the hardware and data taking configuration, summarized in Table I. A combined analysis is performed on all of these datasets.

Detector calibration is performed using line sources that can be inserted along calibration tracks that wrap around each cryostat. Once per week, ^{228}Th sources are deployed into each track, one at a time, for 90 min. In addition, in January 2019, a ^{56}Co line source with a nominal activity of 6 kBq was deployed in each track for one week at a time. This source emits many γ rays with an energy of >1.5 MeV, which produce inherently multisite pair production events that are useful for systematic checks.

III. DETECTION SIGNATURE

The MAJORANA DEMONSTRATOR is searching for the $\beta\beta$ decays of ^{76}Ge to the 0^+_1, 2^+_1, and 2^+_2 states of ^{76}Se, in both 0ν and 2ν decay modes (for a total of six distinct decay modes). The Q-value and γ-ray energies are shown in Fig. 1. The 0^+_1 e.s. decay mode has a Q value of 917 keV and two γs, with energies 559 keV and 563 keV. Due to angular momentum conservation, the γs are emitted with an angular correlation of [39]

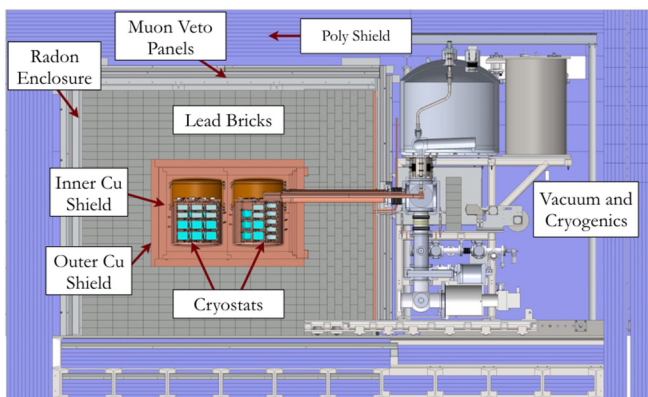$$P(\theta) = 1 - 3\cos^2(\theta) + 4\cos^4(\theta), \qquad (4)$$

TABLE I. A summary of the start dates, key changes, and isotopic exposure of each data set. DS3 and DS4 were run simultaneously on separate DAQ systems, corresponding to Module 1 and Module 2, respectively.

Data set	Start date	Data set distinction	Live time (d)	Exposure (kg yr)
DS1	12/31/15	Inner Cu shield added	74.8	3.11
DS2	5/24/16	Presumming	40.1	1.67
DS3	8/25/16	$M1$ and $M2$ installed	29.9	1.25
DS4	8/25/16	$M1$ and $M2$ installed	19.2	0.62
DS5a	10/13/16	Integrated DAQ (noise)	81.6	6.02
DS5b	1/27/17	Optimized grounding	39.5	2.92
DS5c	3/17/17	Blind	46.2	3.40
DS6a	5/11/17	Presumming, blind	309.8	22.95

where θ is the angle between the emitted γs. The 2_1^+ e.s. decay mode has a Q value of 1480 keV and a single γ, with energy 559 keV. The 2_2^+ e.s. decay mode has a Q value of 823 keV and will release a single 1216 keV γ 36% of the time, or two γs at 657 keV and 559 keV 64% of the time. The 657 keV and 559 keV γs are emitted with an angular correlation of [39]

$$P(\theta) = 1 - 1.218 \cos^2(\theta) + 1.1005 \cos^4(\theta). \qquad (5)$$

These γs are emitted promptly after the $\beta\beta$ decay, and will frequently be absorbed in an active germanium region, resulting in multisite events. Thus, the DEMONSTRATOR can significantly reduce its backgrounds by searching only for events that involve multiple detector hits, as shown in Fig. 3. In particular, we search for events with detector multiplicity of 2 or greater, in which one detector hit falls in a peak at the energy of one of the γs. The data from the detector hit in coincidence with a candidate for a given peak can be used to further reduce backgrounds, as will be described in Sec. III C. A peak-sideband analysis will ultimately be performed in Sec. IV, using simulations to estimate the detection efficiency for each decay mode and to study various sources of systematic error in the detection efficiency. The most likely decay mode to be observed is the $2\nu\beta\beta$ to 0_1^+ e.s., so the figures and
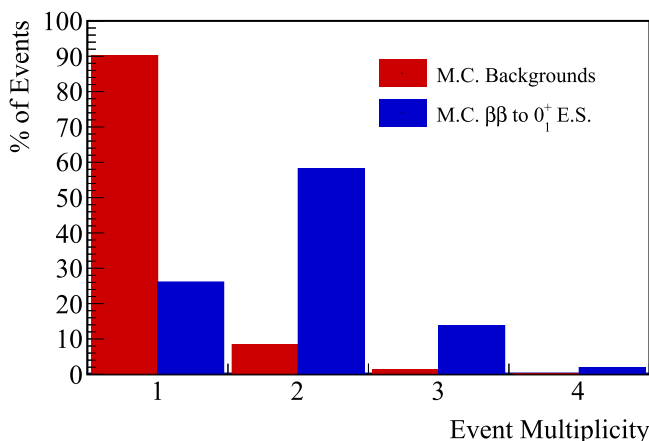

FIG. 3. Comparison of fraction of events with different detector multiplicities from Monte Carlo simulations of backgrounds (red) and $2\nu\beta\beta$ to the 0_1^+ e.s. (blue). Sensitivity can be significantly improved by focusing on events with multiplicity >1.

values cited in this section will focus on this decay; however, the same techniques were applied for all decay modes.

A. Region of interest selection

Events are selected in a signal region of interest (ROI) around the expected γ line energies. The ROI is determined by optimizing the discovery potential for the peak, based on a parametrized peak shape model. The peak shape function is described by a Gaussian component with a low energy tail provided by an exponentially modified Gaussian component [22]. The variation of the peak shape parameters with energy is measured using a simultaneous fit of 26 ^{228}Th calibration γ peaks between 215 keV and 2614 keV. These peak shape parameters and optimal ROIs are measured separately for each dataset listed in Table I.

These peak shapes are further adjusted for gain drift over time and for energy nonlinearities, as described in [22]. In addition to the factors accounted for in the $0\nu\beta\beta$ analysis, detector crosstalk must be accounted for in events involving multiple detector triggers. The effect of crosstalk was measured by comparing the width of the 583 keV peak in multiplicity 1 events, in which no crosstalk is expected, to multiplicity 2 events, in which the 583 keV γ is in coincidence with a γ hit in a second detector that may induce an energy shift due crosstalk. The observed shift in both peak center and FWHM was found to be <0.01 keV.

The signal ROI is then optimized for 3σ-discovery potential based on the peak-shape and background index. For the $2\nu\beta\beta$ to 0_1^+ e.s. decay mode, the ROIs for the 559 and 563 keV γs were 1.6–2 keV wide, depending on the dataset (due to increased noise, DS5a has a wider ROI). The ROI peak containment efficiency was estimated to be 87–89 %.

For each decay mode, a background region of interest (BG ROI) was selected to estimate a background index. The total width of the BG ROIs varied from 50–100 keV depending on the γ energy. These BG ROIs were asymmetric on either side of the peak, and included discontinuities to exclude >99.9% of the peak shape of known background peaks. The signal and BG ROIs selected for each γ peak can be seen in Fig. 11.

B. Simulation of $\beta\beta$ decay to e.s.

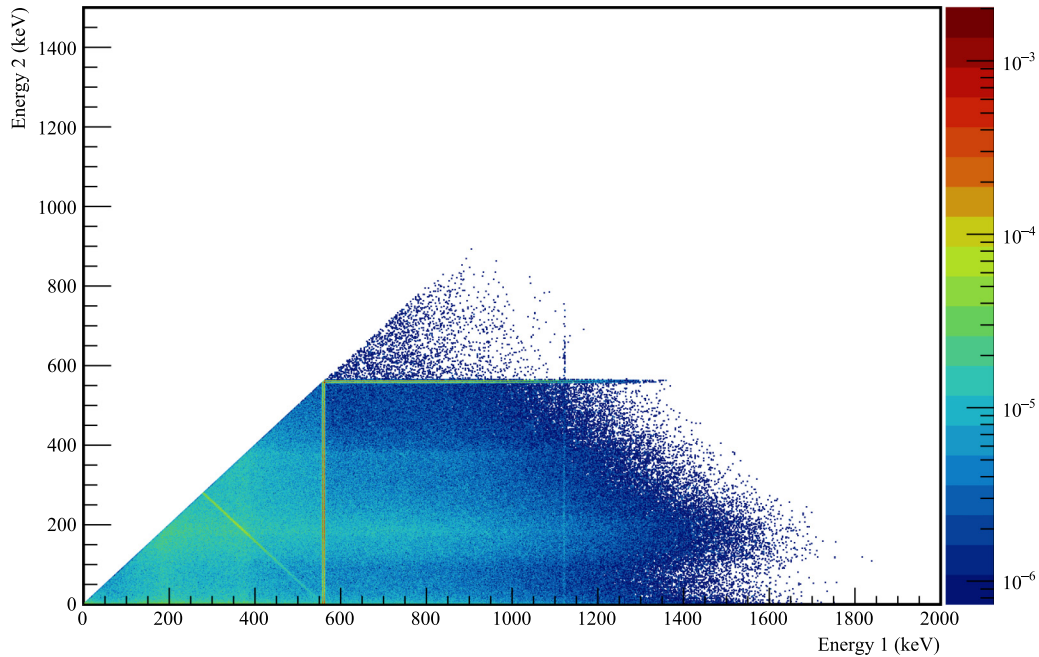MAGE [40], a GEANT4 [41] based simulation package containing a detailed simulated geometry of the MAJORANA

FIG. 4. Multiplicity 2 energy spectrum produced by a simulation of $2\nu\beta\beta$ decay to the 0_1^+ e.s. of ^{76}Se. The vertical and horizontal lines at energies 559 and 563 keV act as a clear detection signature for the decay and are used as a region of interest for this search

DEMONSTRATOR, was used to simulate ^{76}Ge $\beta\beta$-decay events and background events. The $\beta\beta$-decay event generator DE-CAY0 [42] was used in combination with MAGE to produce simulations of each e.s. decay mode for ^{76}Ge, with several modifications. First, DECAY0 was modified for this analysis to include angular correlations in the 2_2^+ e.s. decay mode (the other angular correlation for the 0_1^+ e.s. was already included). Second, the precision of the γ energies was increased from 559 to 559.101 keV, from 563 to 563.178 keV, from 657 to 657.041 keV, and from 1216 to 1216.104 keV [39]. Finally, the seeding for the RANLUX random number generator (RNG) was updated. Previously, a fixed RNG seed was supplied, but a large number of numbers were thrown out to achieve independence; instead, for these simulations an RNG seed based on the job number was supplied. Simulations of each excited state mode were produced, with 5×10^6 events in enriched detectors and 213 993 events in natural detectors, in proportion with the fraction of isotopic mass in each detector group. The multiplicity 2 events from these simulations are shown in Fig. 4.

For each decay mode, multiple sets of simulations were produced for systematic studies. Energy depositions in the lithiated dead layers that extend $\sim$1.1 mm from the surfaces of the crystals will be observed with degraded charge collection, impacting detection efficiency. The dead layer thicknesses for each detector were measured by the vendor prior to insertion into a module, and using the weekly ^{228}Th calibration run data; a combination of these measurements is used by MAGE. Simulations were produced with and without application of dead layers, and the fractional uncertainty from the dead layer measurements was applied to the difference in detection efficiency between both sets of simulations in order to estimate the systematic error from the dead layer thickness.

Dead time was included in two different ways. First, dead time from random, uncorrelated sources such as retrigger dead time, was measured using pulsers injected into the front end electronics for each detector. Additional simulations were produced in which detector hits were dropped with probability equal to the dead fraction in each detector; similarly to the dead layers, the fractional uncertainty from the dead fraction measurements were applied to the differences between these simulations to determine the systematic error. In addition, many detectors were disabled for periods of time; as a result, each dataset is further divided into sub-datasets corresponding to the set of detectors enabled. Sets of simulations were produced for each sub-dataset, and the exposure-weighted average of the simulated detection efficiency was used to obtain a limit. The detection efficiency for various sub-datasets can vary by a factor of >2 from the mean in some sub-datasets, as shown in Fig. 5; this approach entirely corrects for this variation.

C. Background cuts

To further improve detection sensitivity, a variety of background cuts are used. Many of these cuts utilize information from the detectors in coincidence with a $\beta\beta$ decay to e.s. candidate.

(i) The same run selection and data cleaning cuts applied in [22,43] were applied here, excluding runs taken prior to the installation of the inner copper shield. Data cleaning routines remove waveforms caused by nonphysical processes such as transient noise, and events that cannot be reliably analyzed such as pileup and saturated waveforms. The combined effect of data
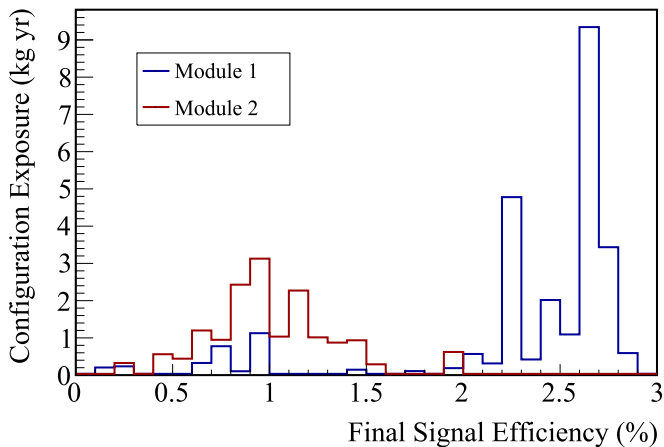
FIG. 5. The datasets were further divided into 80 sub-datasets based on which detectors were active, and the isotopic exposure and detection efficiency for each $\beta\beta$ to e.s. mode were separately calculated for each one. Shown above is the distribution of detection efficiencies for the decay to the 0_1^+ e.s.

cleaning cuts is to remove $<0.1\%$ of physical background events.

  (ii) As already discussed, events with a detector multiplicity of one are removed. For e.s. decay modes with a single γ, events with detector multiplicity >2 are also cut. Detector multiplicity is determined by grouping together waveforms in a 4 μs rolling window into events. This window is conservative, as $<0.1\%$ of true coincidence events are expected to trigger >1 μs apart. Events were divided based on which module they occurred in; events with energy deposition in both modules were cut. This enables an independent analysis to be performed for each module.

(iii) Events associated with cosmic ray muons are cut by vetoing events near in time to triggers of the muon veto system. The muon veto consists of scintillating panels with 4π coverage of the modules, and triggers when at least two panels on different surfaces simultaneously surpass an energy threshold. Events are cut within 20 ms before and 1 s after a muon event; this window is expected to remove $>99.9\%$ of muon-associated events. The effect of this cut on the $\beta\beta$ decay to e.s. half-life measurement is evaluated by subtracting the veto time windows from the exposure, rather than by simulating its effect on the detection efficiency. This cut removes $<0.1\%$ of live time.

(iv) Events are cut in which no hit in coincidence with a hit in the BG or signal ROI is enriched in ^{76}Ge. One of the coincident detectors is assumed to contain the site of the $\beta\beta$ decay; since $\sim95\%$ of the isotopic mass of ^{76}Ge is contained in enriched detectors, this cut sacrifices $<5\%$ of $\beta\beta$ to e.s. events, while cutting a significantly higher fraction of backgrounds due to the relatively higher fraction of total mass in these detectors, and since they were preferentially placed closer to the outside of the detector arrays.

  (v) Events where any coincident detector or the sum energy over all detectors have energy within a set of energy ranges are cut. The motivation for this cut is to remove background γs with known energies that either Compton scatter (for the sum energy cut) or are emitted in a γ cascade (for the coincident energy cut). In addition, the energy spectrum produced by Compton scattering of γ rays has finite amplitude at low energies, while the $\beta\beta$ spectral amplitude runs to 0 at low energies. For this reason, a low energy threshold is also set by this cut. Because the energy spectrum in coincident enriched and natural detectors is expected to differ due to the different isotopic abundances of ^{76}Ge, a separate set of energy ranges is used for each. The energy ranges are selected using an optimization process described below. For $0\nu\beta\beta$ to e.s. decay modes with a single γ, a coincident energy window equal to the Q value of the decay is used in lieu of the optimization process.

A simulation of the background spectrum measured by the DEMONSTRATOR was used to optimize sensitivity to $\beta\beta$ decay to e.s. using these cuts. MAGE simulations of known backgrounds from a variety of decay chains generated in the physical components of the experiment as defined within MAGE were used. The activities of the components included were determined using an unpublished fit of a linear combination of background spectra to data that is part of a background study that is still in progress; the early model used is known to be incomplete [44]. Figure 6 shows the two-dimensional energy spectrum for events with multiplicity >2, along with a comparison to data. This background model includes as background sources a limited number of components with γ rays from ^{40}K, ^{60}Co, ^{222}Rn, ^{232}Th, ^{238}U, and ^{68}Ge. One missing component of this model is cosmogenically activated ^{60}Co inside of the natural HPGe detectors, which produces multidetector events with high likelihood, and contribute to the 1173 and 1333 keV peaks in the hit energy spectrum. Fortunately, the accuracy of the result presented in Sec. IV is not impacted by deficits in the background model used, as it assumes a flat background; still, improving this background model would help in optimizing the result.

An algorithm was written that selects a set of coincident and sum energy ranges in order to optimize the discovery potential as predicted by the background model simulation. The algorithm begins by identifying candidate events in the BG and signal ROIs in both the background model and $\beta\beta$ decay to e.s. decay simulations. These events are then sorted into energy bins for each coincident hit and for the event sum energy (a single event will fall into multiple bins). We want to cut an energy bin if doing so improves our discovery potential, meaning, for bin k,

$$\frac{DP(sN_{BG})}{N_{sig}} < \frac{DP(s(N_{BG} - n_{BG,k}))}{N_{sig} - n_{sig,k}}. \qquad (6)$$

DP is the 3σ discovery potential, defined as the signal strength for which we have a 50% chance of claiming 3σ discovery, based on the Poisson counting statistics of the signal and background events; N_{sig} and N_{BG} are the number of counts
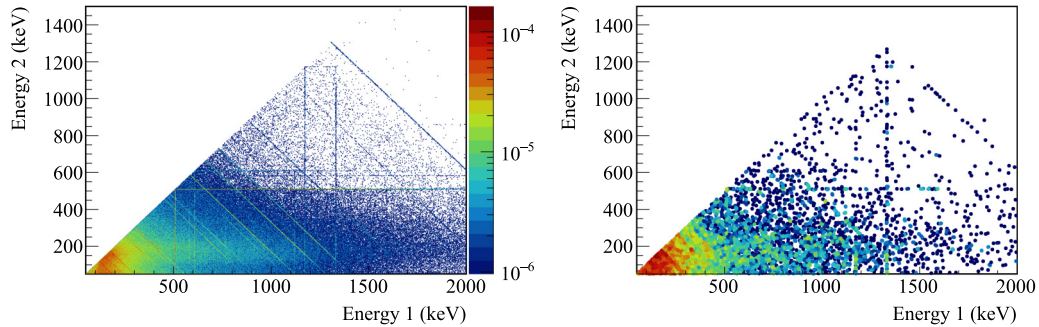
FIG. 6. Left: simulated multiplicity 2 background two-dimensional energy spectrum histogram. Vertical and horizontal lines correspond to events in which one hit has a fixed energy, while diagonal lines correspond to events with a fixed sum energy. Right: Scatter plot of all multiplicity 2 events, including all events in datasets used in this analysis. A Gaussian kernel density estimate with width 5 keV was used to achieve a similar color scale to the simulated spectrum.

in the simulated ROIs for the e.s. decay and the background model; $n_{\mathrm{sig},k}$ and $n_{BG,k}$ are the number of simulated e.s. and background counts removed by cutting events in an energy bin; s is a scaling factor for the background to reflect the expected measured background counts. The scaling factor is determined using the ratio of events in the BG ROI in un-blinded data to those found in simulations, and then increased to reflect the additional exposure from blinded data; for the $\beta\beta$ to 0_1^+ e.s. decay mode, s had a value of 0.001. For each bin, we will calculate the probability that Eq. (6) holds based on Poisson counting statistics for $n_{BG,k}$ and $n_{\mathrm{sig},k}$. The bin with the highest probability of improving discovery potential is then added to the cut. After this, cut events are removed from other bins, the probability of improvement in discovery probability is recalculated, and the process is repeated until no bin has a >50% chance of improving the cut.

The sampling statistics for the background modeling simulation are limited due to the very low probability of an event primary producing a multidetector event. As a result, this process is biased to cut energy bins with an upward fluctuation in background counts, causing it to cut more events than optimal. In order to counter this bias, a penalty term is added to the probability above so that a new energy range will only be introduced to the cut if there is a 99.8% chance that cutting it will improve discovery potential. This penalty term is similar to the one applied when using the Akaike information criterion (AIC) [45]. To ensure that the bin contents are large enough to overcome this penalty, a bin width of 6.4 keV is initially used in determining this cut. The energy ranges selected are then modified by reducing the bin width by a factor of 2 at a time in order to improve the energy resolution of the cut, with a final binning of width 0.2 keV.

The end result of this cut optimization routine can be seen in Figs. 7, 8, and 10. The combination of the energy and enriched source detector cuts is expected to remove 82% of Module 1 background events and 87% of Module 2, while sacrificing 41% and 49% of $\beta\beta$ to 0_1^+ e.s. events in Modules 1 and 2, respectively. The systematic error on the sacrifice for the enriched source detector cut is determined based on the uncertainty in the total isotopic mass in the enriched and natural detectors, and was found to be <0.1%. Systematic error in the sum and coincident energy cuts can originate

from spectral distortions that may shift events in and out of cut regions. Various spectral distortions were investigated, including energy nonlinearities and error in the phase space factor for $\beta\beta$ decay. Ultimately, the largest possible source of error was determined to be the phase space integral, for which Kotila and Iachello reported an fractional uncertainty of 0.5% [13]. Here, we take a conservative approach and apply this as the uncertainty for this cut efficiency; this is equivalent to assuming that all of the error in phase space calculations is concentrated in either events that are cut or uncut. Even so, the systematic uncertainties applied to these cut efficiencies are subdominant to other sources.

D. Simulation validation

To validate the simulated detection efficiency for $\beta\beta$ decay to e.s., measurements of pair-production peaks were compared between simulations and calibration data. Pair-production events involve the production of an e^+-e^- pair in the bulk of a detector, and the prompt emission of two 511 keV γs from the e^+ annihilation. Because these events involve a single pair production site and the prompt emission of γs which may be absorbed in a separate detector, they make a good proxy for $\beta\beta$ decay to e.s. events. In single-escape peak (SEP) events, one γ is absorbed in the detector containing the pair production, while the other escapes, resulting in a source detector hit with energy equal to the γ energy minus 511 keV. In double-escape peak (DEP) events, both γs escape the detector, resulting in a source detector hit with energy equal to the γ energy minus 1022 keV. Both SEP and DEP events present the possibility for a second 511 keV detector hit. By comparing the rate of multiplicity-1 events in the SEPs and DEPs to the rate of multiplicity-2 events in which one hit falls into one of these peaks and the other falls into the 511 keV peak, we can measure a proxy for the detection efficiency of our multidetector event signature. ^{56}Co produces a large number of γs at energies high enough to cause pair production, which allows for a comparison of many peaks to our simulation. This comparison was performed using 168.1 h and 167.1 h of data with the ^{56}Co line source inserted into the Module 1 and Module 2 calibration tracks, respectively, and a simulation of 3×10^9 event primaries generated by MaGe.

(a) Simulated background coincident energy spectrum

(b) Simulated background sum energy spectrum

(c) Simulated $2\nu\beta\beta$ to 0_1^+!E.S. coincident energy spectrum

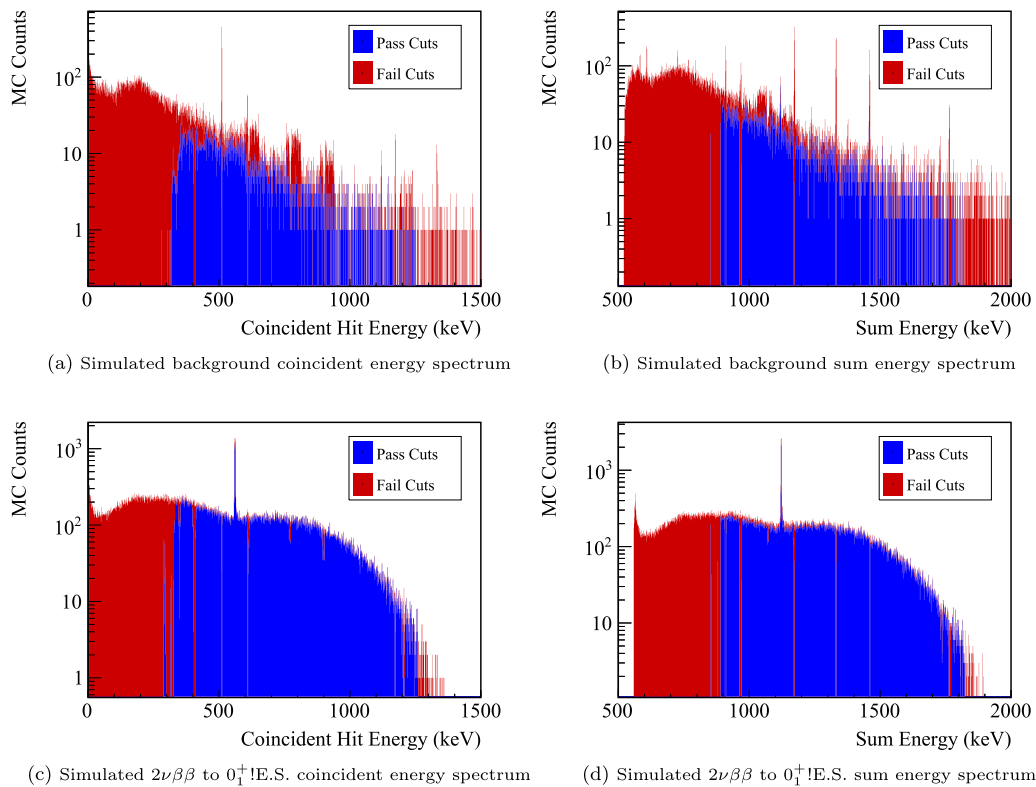(d) Simulated $2\nu\beta\beta$ to 0_1^+!E.S. sum energy spectrum

FIG. 7. Energy spectra demonstrating the effects of applying the sum- and coincident-energy cuts for the $2\nu\beta\beta$ decay to 0_1^+ decay mode. All multiplicity 2 or greater events are included, with passing events in blue and cut events stacked atop these in red. Left: Energy spectrum for all BG (top) and e.s. (bottom) simulated hits in coincidence with a hit in the signal or BG ROI. Right: Sum energy spectrum for BG (top) and e.s. (bottom) simulated events including a hit in the signal or BG ROI. Figure 8 shows similar information, including only multiplicity 2 events and plotted over two dimensions; this includes the cyan and green events in that figure, projected along the single-hit or sum energies. Note in the BG spectra that narrow ranges around prominent peaks are cut, as intended.

The result of this comparison is shown in Fig. 9, with an overall offset that cannot be fully explained by statistical error. Some of this discrepancy can be explained by uncertainty in the dead layer thickness; the remaining difference represents systematic error from an unknown source such as errors in the MAGE geometry. A systematic error term is added to the detection efficiencies until these results are consistent. The error terms are 0.20% for Module 1 and 0.47% for Module 2, which are added to the detection efficiencies for $\beta\beta$ to e.s. The measured error in Module 1 was found to be consistent with the expected error from dead layers, which was not the case for Module 2; for this reason, Module 2 has a much larger error term which will be the dominant error in the $\beta\beta$ to e.s. efficiencies.

E. Simulated detection efficiency

The detection efficiency for $\beta\beta$ decay to e.s. is calculated by applying the previously mentioned cuts to the simulations of each $\beta\beta$-decay mode. Table II lists the effect of each source of signal loss described in this section, determined using simulations. For each source of signal loss, the systematic uncertainty estimations described in the previous subsections are listed. These uncertainties are assumed to be Gaussian and uncorrelated, and they are combined by adding the fractional uncertainties in quadrature. The dominant sources of uncer-

tainty come from the dead layer thickness and the error found in the ^{56}Co spectral comparisons. Using these simulations, the detection efficiency for the $2\nu\beta\beta$ to 0_1^+ e.s. decay mode was estimated to be $2.3 \pm 0.2\%$ for Module 1 and $1.0 \pm 0.2\%$ for Module 2. The primary reason Module 1's detection efficiency is greater than Module 2's is that Module 2 has more disabled detectors than Module 1.

IV. RESULTS

Data collected between January 12, 2016 and April 17, 2018 were used for this analysis. The total isotopic exposure was 25.819 ± 0.037 kg yr for Module 1 and 16.104 ± 0.024 kg yr for Module 2. Isotopic exposure is defined here as the total mass of ^{76}Ge in a module times the run time for the module. This stands in contrast with the DEMONSTRATOR's $0\nu\beta\beta$ result [22], which subtracts dead layers and inactive detectors from the mass used to calculate active isotopic exposure; instead, as previously described, inactive isotopic material is instead accounted for in the detection efficiency.

Of this exposure, 12.463 kg yr in Module 1 and 8.232 kg yr in Module 2 consisted of blinded data. Data were unblinded in a staged fashion; first, multiplicity 1 data excluding hits below 200 keV and hits in the $0\nu\beta\beta$ region of interest were unblinded. Events with multiplicity 2 or greater were unblinded for this analysis after review of the unblinded results, which
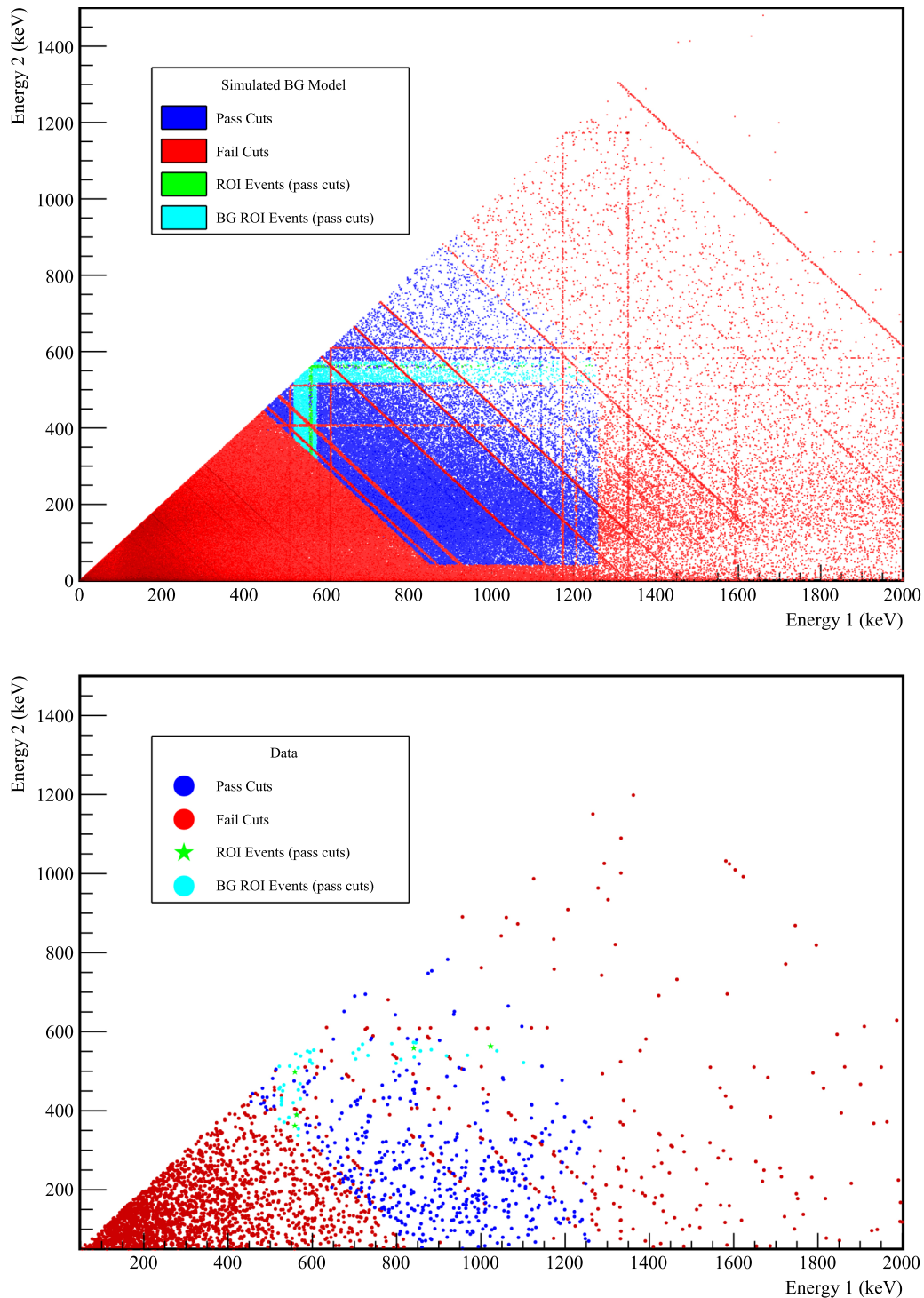
FIG. 8. Top: Simulated multiplicity 2 energy spectrum for the background model. The colors represent cut events (red), surviving events (blue), and events that pass all cuts in the signal ROI (green) and BG ROI (cyan). Figure 7 shows similar information, with the events in the green and cyan ROIs projected onto the single hit (vertical and horizontal) and sum energy (diagonal) axes. Bottom: scatter plot of multiplicity 2 events in data used in this analysis.

have been publicly presented [46] but not published in a peer reviewed journal. Immediately after unblinding, an error in the application of detector selection was detected based on irregularities in the rates of high-multiplicity events; this was fixed prior to analyzing the data for $\beta\beta$ decay to e.s. Addi-

tionally, after performing an unblinded analysis, two errors were uncovered in DECAY0. First, the incorrect γ correlation factors were used for the 2_2^+ e.s. decay mode; second, for correlated γ emissions, the RNG used was not using the seed provided to the program. These errors were rectified in the
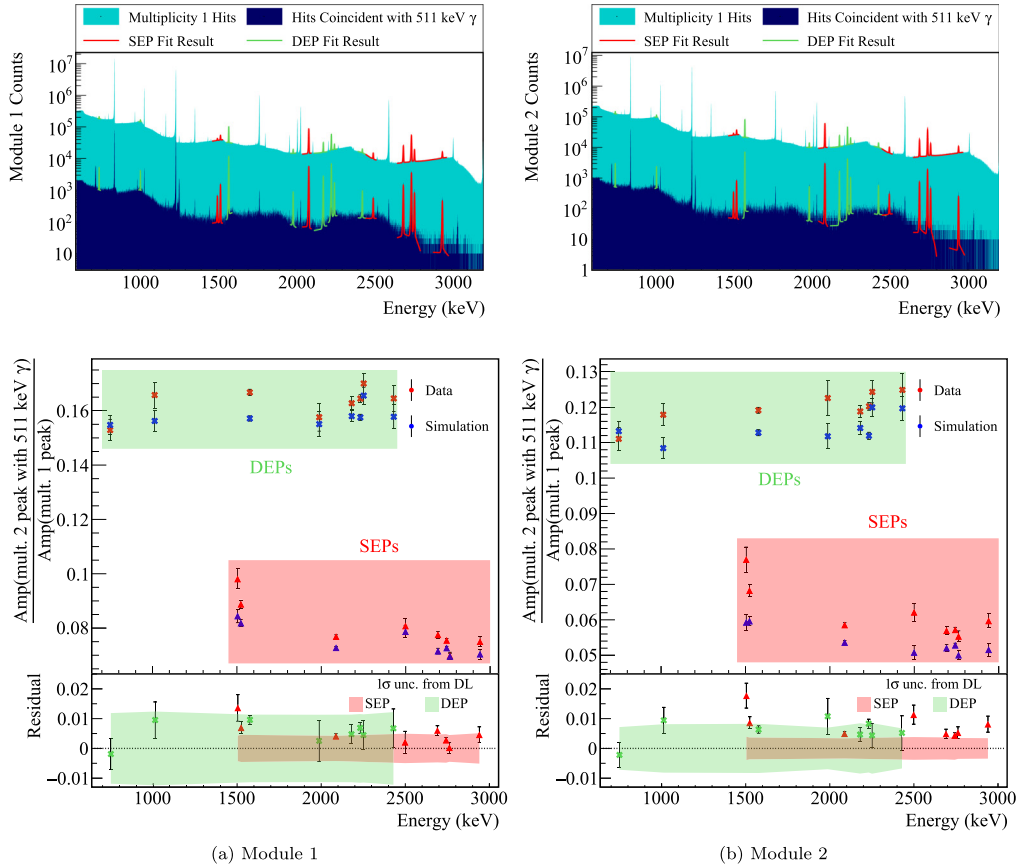
(a) Module 1   (b) Module 2

FIG. 9. Top: Energy spectra recorded while the ^{56}Co line source was inserted into the calibration track for Module 1 (left) and Module 2 (right). Spectra are shown for multiplicity 1 events and multiplicity 2 events in which the other detector hit fell within the 511 keV peak. The SEPs (red triangle) and DEPs (green x) that were fit and used for simulation validation are shown. Bottom: the ratio of peak amplitudes from the selected SEPs and DEPs for Module 1 (left) and Module 2 (right). The expected systematic error from the dead layer thickness for SEPs and DEPs is shown on top of the residuals.

simulations without any changes to data selection; the detection efficiency was recalculated and agreed with the old values within uncertainty.

Figure 10 shows data around the 559 and 563 keV ROIs for the $2\nu\beta\beta$ decay to 0_1^+ e.s. decay mode including the effect of cuts, compared with the background model simulation.

The 511 keV peak from e^+ annihilation is notably wider in data than in the simulation; this can be explained by doppler broadening, which is not included in the MAGE simulation.

A frequent analysis was performed to calculate Neyman confidence intervals for the half-life of each $\beta\beta$ decay to e.s. decay mode. For a given decay peak k, we can calculate the
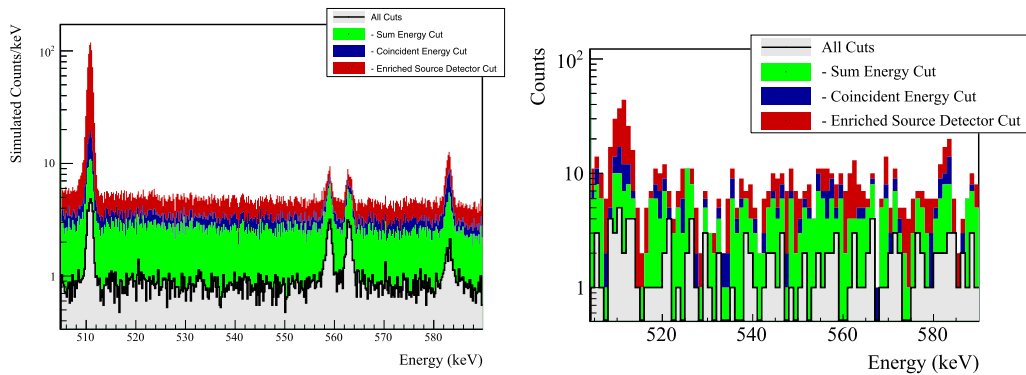

FIG. 10. Left: Simulated energy spectrum including 42 kg yr of exposure from the background model and the $2\nu\beta\beta$ decay to 0_1^+ e.s. peaks at 559 and 563 keV, assuming a half-life of 10^{24} y. The cuts optimized for this decay mode are included. Right: Measured data energy spectrum with the same cuts applied.

TABLE II. Detection efficiency for the $2\nu\beta\beta$ to 0_1^+ e.s. mode. The first entry is the efficiency prior to applying cuts and other effects. The efficiency for individual effects is listed as if it was the last effect applied; as a result, since these effects are not statistically independent, their product as listed will not be the final efficiency. Uncertainties shown are determined from systematics measurements described in the text.

Source	Module 1 efficiency	Module 2 efficiency	Dominant source of uncertainty
Multidetector with Full energy γ	$5.6 \pm 0.2\%$	$3.1 \pm 0.5\%$	^{56}Co validation measurement
ROI containment	$86.8 \pm 1.5\%$	$86.8 \pm 1.5\%$	Energy calibration and resolution systematics
Dead layer	$74.7 \pm 4.3\%$	$63.8 \pm 6.3\%$	Dead layer thickness
Detector dead times	$98.3 \pm 0.8\%$	$98.4 \pm 0.8\%$	Detector dead time
Enriched source detector cut	$96.9 \pm\ <0.1\%$	$90.6 \pm\ <0.1\%$	Detector mass and isotopic abundance
Coincident energy cut	$91.4 \pm 0.5\%$	$89.7 \pm 0.5\%$	Phase space integral
Sum energy cut	$62.8 \pm 0.5\%$	$56.4 \pm 0.5\%$	Phase space integral
Final efficiency	$2.33 \pm 0.17\%$	$1.01 \pm 0.18\%$	

expected number of counts in the signal ROI using

$$\langle s_k \rangle = \ln 2 \frac{N_A}{m_{76}} \epsilon_k \frac{M_{iso} T_{live}}{T_{1/2}}, \quad (7)$$

where N_A is Avogadro's number, m_{76} is the isotopic mass of ^{76}Ge, ϵ_k is the detection efficiency for the peak, $M_{iso} T_{live}$ is the isotopic exposure, and $T_{1/2}$ is the half-life of the decay mode. For convenience, we will define

$$T_k^* = \ln 2 \frac{N_A}{m_{76}} \epsilon_k M_{iso} T_{live}, \quad (8)$$

which is the decay half-life that would produce on average one count in signal ROI k. The following likelihood function is used:

$$\mathcal{L}_k(T_{1/2}, T_k^*, b_k | n_k, m_k, \langle T_k^* \rangle, \sigma_{T_k^*}, \tau)$$

$$= \frac{\mu_k^{n_k} e^{-\mu_k}}{n_k!} \frac{(b_k/\tau)^{m_k} e^{-b_k/\tau}}{m_k!} \frac{1}{\sigma_{T_k^*}\sqrt{2\pi}} e^{-\frac{(T_k^* - \langle T_k^* \rangle)^2}{2\sigma_{T_k^*}^2}}, \quad (9)$$

$$\mu_k = s_k + b_k = \frac{T_k^*}{T_{1/2}} + b_k.$$

In this likelihood function, $T_{1/2}$ is the half-life of the decay, T_k^* is defined in Eq. (8) and assumes Gaussian statistics, and b_k, s_k, and μ_k are the expected number of background, signal, and total counts in the signal ROI assuming Poisson statistics. As input parameters, n_k and m_k are the observed counts in the signal and BG ROIs, respectively, $\langle T_k^* \rangle$ and $\sigma_{T_k^*}$ are the measured value and uncertainty on T_k^* calculated from the signal efficiency and exposure, and τ is a ratio used to compute the expected number of backgrounds in the signal ROI ($b_k \tau$). In order avoid double counting, events with multiple hits in either the signal or BG ROI only add one count to n_k and m_k, respectively. If an event has a hit in both the signal and BG ROIs, then it is only counted as in n_k; the small excess this creates in the signal ROI is accounted for in τ.

The likelihood function is maximized over T_k^* and b_k as prescribed by Rolke [47] in order to produce a 90% confidence interval for each individual peak-module combination. A combined result is then calculated for each decay mode by constructing a likelilhood from the product of Eq. (9). Confidence intervals were calculated by profiling the negative log likelihood along $T_{1/2}^{-1}$ until it increased by 2.7. For all

modes, the 90% confidence intervals were bounded at $T_{1/2}^{-1} = 0$, meaning that lower half-life limits are presented.

The detection sensitivity is computed by constructing a toy Monte Carlo for each decay mode, assuming that each $T_{1/2}^{-1} = 0$. For each sample i, a random n_i and m_i is drawn from a Poisson distribution with mean b_k and m_k. The confidence interval for a measurement with these values is computed. The median sensitivity is extracted by taking the median lower half-life limit over 100 001 samples.

Table III contains a summary of the results for each decay mode. For the $2\nu\beta\beta$ decay to 0_1^+ e.s. mode, five events passed all cuts in the combined 559 and 563 keV signal ROIs, with 4.2 events expected from backgrounds. This set a 90% CI limit on the half-life of $T_{1/2} > 7.5 \times 10^{23}$ y, compared with a 90% median sensitivity of $T_{1/2} > 1.05 \times 10^{24}$ y. Figure 11 shows the events that passed all cuts for all $\beta\beta$ decay to e.s. γ peaks, with the signal and BG ROIs highlighted.

Discussion of results

This result sets the most stringent limits and has the greatest sensitivity to date for $\beta\beta$ decay of ^{76}Ge to all excited states of ^{76}Se. Table IV lists the previous best limits along with those set by this work. The MAJORANA DEMONSTRATOR derives its increased sensitivity relative to the results from GERDA Phase I [27] from several factors. First, the DEMONSTRATOR had higher detection efficiency due to the lack of liquid argon surrounding the detectors, which shielded the deexcitation γs. Second, the dominant background in GERDA's search for excited state decays came from cosmogenic ^{42}K in its liquid argon shield, which does not exist in the DEMONSTRATOR. Finally, the DEMONSTRATOR had significantly better energy resolution due to the lack of crosstalk between detectors, which worsened GERDA's resolution for multidetector events.

This result has also begun to probe recent theoretical predictions for the half-life for $2\nu\beta\beta$ to the 0_1^+ e.s. of ^{76}Se. A recent half-life prediction using renormalized proton-neutron quasirandom phase approximation (RQRPA) of $(1.2-5.8) \times 10^{23}$ y [27] has been excluded with CL 97% by this result. Combining the best measurement of the $2\nu\beta\beta$ to g.s. half-life [27] and phase-space integrals [14] with nuclear matrix element calculations applying an effective field theory (EFT)

TABLE III. Results for all decay modes. n_k and m_k are the observed counts in the signal and BG ROI, respectively, and can be seen, combining modules, in Fig. 11. The expected ROI BGs corresponds to τm_k from Eq. (9). ϵ is the final signal detection efficiency measured from simulations as shown in Table II. $\langle T_k^* \rangle$ is the value calculated from exposure and efficiency estimations, as defined in Eq. (8).

Decay mode	Peak	Module	n_k	m_k	Expected ROI BGs	ϵ (%)	$\langle T_k^* \rangle$ ($\times 10^{23}$y)	$T_{1/2}$ ($\times 10^{23}$y) 90% limit	$T_{1/2}$ ($\times 10^{23}$y) 90% sensitivity
$0^+_{g.s.} \xrightarrow{2\nu\beta\beta} 0^+_1$	559 keV	$M1$	2	51	1.77	1.2	16.5 ± 1.2	>4.6	>5.1
		$M2$	1	6	0.25	0.5	4.5 ± 0.8	>1.3	>3.2
	563 keV	$M1$	2	51	1.95	1.2	16.5 ± 1.2	>4.9	>5.1
		$M2$	0	6	0.22	0.5	4.4 ± 0.8	>3.2	>3.2
	Combined							>7.5	>10.5
$0^+_{g.s.} \xrightarrow{2\nu\beta\beta} 2^+_1$	559 keV	$M1$	0	35	1.43	1.4	19.2 ± 2.0	>14.1	>7.8
		$M2$	1	2	0.10	0.6	5.2 ± 1.7	>1.2	>3.3
	Combined							>7.7	>10.2
$0^+_{g.s.} \xrightarrow{2\nu\beta\beta} 2^+_2$	559 keV	$M1$	3	74	2.57	1.0	13.8 ± 1.7	>3.2	>4.3
		$M2$	1	8	0.32	0.4	3.8 ± 1.7	>0.7	>2.3
	657 keV	$M1$	0	46	1.48	0.8	11.2 ± 1.5	>8.2	>4.6
		$M2$	0	6	0.19	0.4	3.1 ± 1.6	>1.8	>1.8
	1216 keV	$M1$	0	41	1.07	0.4	5.8 ± 1.6	>4.0	>2.1
		$M2$	0	7	0.24	0.2	1.5 ± 1.8	>2.2	>2.2
	Combined							>12.8	>8.2
$0^+_{g.s.} \xrightarrow{0\nu\beta\beta} 0^+_1$	559 keV	$M1$	0	6	0.24	1.5	21.5 ± 1.8	>15.8	>15.8
		$M2$	0	1	0.06	0.6	5.7 ± 1.1	>4.1	>4.1
	563 keV	$M1$	0	6	0.25	1.5	21.2 ± 1.8	>15.6	>15.6
		$M2$	0	1	0.06	0.6	5.7 ± 1.1	>4.1	>4.1
	Combined							>39.9	>39.9
$0^+_{g.s.} \xrightarrow{0\nu\beta\beta} 2^+_1$	559 keV	$M1$	0	0	0.00	1.6	22.9 ± 2.5	>16.8	>16.8
		$M2$	0	0	0.00	0.7	6.0 ± 2.1	>4.0	>4.0
	Combined							>21.2	>21.2
$0^+_{g.s.} \xrightarrow{0\nu\beta\beta} 2^+_2$	559 keV	$M1$	0	11	0.40	1.0	13.8 ± 1.8	>10.0	>10.0
		$M2$	1	1	0.07	0.4	3.7 ± 1.8	>0.6	>2.2
	657 keV	$M1$	1	10	0.41	0.9	13.5 ± 1.9	>4.1	>9.8
		$M2$	0	1	0.01	0.4	3.5 ± 1.8	>2.0	>2.0
	1216 keV	$M1$	0	0	0.00	0.4	6.2 ± 1.7	>4.3	>4.3
		$M2$	0	0	0.00	0.2	1.6 ± 1.9	>0.3	>0.3
	Combined							>9.7	>18.6

framework [51] and interacting boson model [52], yield half-life predictions of 1.7×10^{24} y and 7.1×10^{24} y, respectively.

More progress will still be required to test half-life predictions for $2\nu\beta\beta$ to the 2^+ e.s. of ^{76}Se. The most recent predictions for the 2^+_1 e.s. range using RQRPA [53–56] and EFT [51] techniques yield half-lives in excess of 1.0×10^{26} y, well beyond the reach of the MAJORANA DEMONSTRATOR.

TABLE IV. Table of limits at 90% CL for each $\beta\beta$ decay to e.s. decay mode.

Decay mode	Previous limit	MJD limit
$0^+_{g.s.} \xrightarrow{2\nu\beta\beta} 0^+_1$	3.7×10^{23} y [27]	7.5×10^{23} y
$0^+_{g.s.} \xrightarrow{2\nu\beta\beta} 2^+_1$	1.6×10^{23} y [27]	7.7×10^{23} y
$0^+_{g.s.} \xrightarrow{2\nu\beta\beta} 2^+_2$	2.3×10^{23} y [27]	1.3×10^{24} y
$0^+_{g.s.} \xrightarrow{0\nu\beta\beta} 0^+_1$	1.3×10^{22} y [48]	4.0×10^{24} y
$0^+_{g.s.} \xrightarrow{0\nu\beta\beta} 2^+_1$	1.3×10^{23} y [49]	2.1×10^{24} y
$0^+_{g.s.} \xrightarrow{0\nu\beta\beta} 2^+_2$	1.4×10^{21} y [50]	9.7×10^{23} y

Similarly, a calculation using RQRPA for the 2^+_2 e.s. yielded a half-life in excess of 7×10^{27} y [53]. Without knowledge of $|m_{\beta\beta}|$ or other BSM physics parameters involved in generating $0\nu\beta\beta$, it is impossible to generate a specific half-life prediction for neutrinoless decay modes to e.s. By applying nuclear matrix elements calculated for $0\nu\beta\beta$ to the 0^+_1 e.s. under the assumption of light neutrino exchange, we can calculate upper limits on $|m_{\beta\beta}|$ of 3.2–7.7 eV [57,58].

This analysis leaves some room for improvement; for example, by taking advantage of the PPC detectors' sensitivity to events that are multisite within a single detector [32], we could refine the search to achieve greater signal acceptance. In fact, one could potentially use pulse-shape information to change the signal selection criterion to include single-detector events in which a de-excitation γ is absorbed in the same detector as the $\beta\beta$ site, which could greatly improve signal acceptance. Furthermore, the MAJORANA DEMONSTRATOR is continuing to collect data. A future analysis, with increased exposure and improved signal sensitivity, may be able to test the effective field theory prediction.
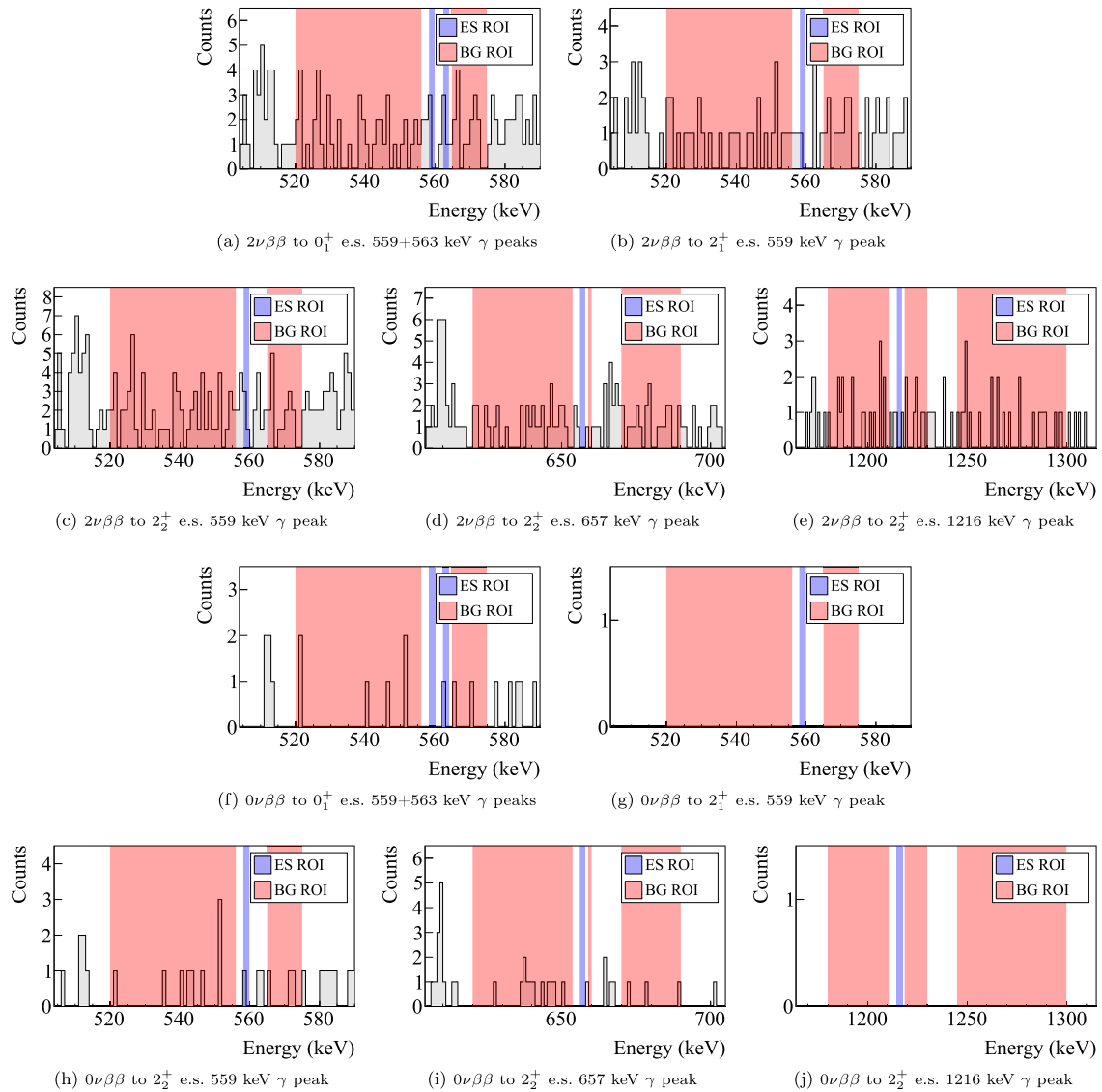
FIG. 11. Energy spectra for each $\beta\beta$ decay to e.s. decay mode after applying optimized cuts. The signal and BG ROIs are highlighted in blue and red, respectively.

[1] M. Goeppert-Mayer, Phys. Rev. **48**, 512 (1935).

[2] W. H. Furry, Phys. Rev. **56**, 1184 (1939).

[3] F. T. Avignone, S. R. Elliott, and J. Engel, Rev. Mod. Phys. **80**, 481 (2008).

[4] J. D. Vergados, H. Ejiri, and F. Šimkovic, Rep. Prog. Phys. **75**, 106301 (2012).

[5] H. Päs and W. Rodejohann, New J. Phys. **17**, 115010 (2015).

[6] S. Dell'Oro, S. Marcocci, M. Viel, F. Vissani, and S. Goswami, Adv. High Energy Phys. **2016**, 2162659 (2016).

[7] M. J. Dolinski, A. W. Poon, and W. Rodejohann, Annu. Rev. Nucl. Part. Sci. **69**, 219 (2019).

[8] E. Majorana, Il Nuovo Cimento (1924-1942) **14**, 171 (2008).

[9] J. Schechter and J. W. F. Valle, Phys. Rev. D **25**, 2951 (1982).

[10] A. D. Sakharov, Pisma Zh. Eksp. Teor. Fiz. **5**, 32 (1967) [Sov. Phys. Usp. **34**, 392 (1991)].

[11] M. Fukugita and T. Yanagida, Phys. Lett. B **174**, 45 (1986).

[12] J. Suhonen, Phys. Rev. C **96**, 055501 (2017).

[13] J. Kotila and F. Iachello, Phys. Rev. C **85**, 034316 (2012).

[14] S. Stoica and M. Mirea, Frontiers in Physics **7**, 12 (2019).

[15] J. Engel and J. Menéndez, Rep. Prog. Phys. **80**, 046301 (2017).

[16] A. Barabash, Nucl. Phys. A **935**, 52 (2015).

[17] A. Barabash, F. Avignone, J. Collar, C. Guerard, R. Arthur, R. Brodzinski, H. Miley, J. Reeves, J. Meier, K. Ruddick, and V. Umatov, Phys. Lett. B **345**, 408 (1995).

[18] A. S. Barabash, F. Hubert, P. Hubert, and V. I. Umatov, JETP Lett. **79**, 10 (2004).

[19] A. S. Barabash, P. Hubert, A. Nachab, and V. I. Umatov, Phys. Rev. C **79**, 045501 (2009).

[20] A. S. Barabash, in *Workshop on Calculation of Double-Beta-Decay Matrix Elementa (MEDEX'17)*, edited by O. Civitarese, I. Stekl, and J. Suhonen, AIP Conf. Proc. No. 1894 (AIP, New York, 2017), p. 020002.

[21] N. Abgrall *et al.* (Majorana Collaboration), Adv. High Energy Phys. **2014**, 365432 (2014).

[22] S. I. Alvis *et al.* (Majorana Collaboration), Phys. Rev. C **100**, 025501 (2019).

[23] M. Agostini *et al.* (GERDA Collaboration), Science **365**, 1445 (2019).

[24] M. Agostini *et al.* (GERDA Collaboration), Phys. Rev. Lett. **125**, 252502 (2020).

[25] N. Abgrall *et al.*, in *Workshop on Calculation of Double-Beta-Decay Matrix Elementa (MEDEX'17)*, edited by O. Civitarese, I. Stekl, and J. Suhonen, AIP Conf. Proc. No. 1894 (AIP, New York, 2017), p. 020027.

[26] E. Fiorini, in *Proceedings of the International Conference Neutrino '77*, Vol. 2 (Akademy of Sciences of USSR, Moscow, 1978), pp. 315–320.

[27] M. Agostini *et al.* (GERDA Collaboration), J. Phys. G: Nucl. Part. Phys. **42**, 115201 (2015).

[28] A. Dolgov and A. Smirnov, Phys. Lett. B **621**, 1 (2005).

[29] A. Barabash, A. Dolgov, R. Dvornický, F. Šimkovic, and A. Smirnov, Nucl. Phys. B **783**, 90 (2007).

[30] F. Šimkovic and A. Faessler, Prog. Part. Nucl. Phys. **48**, 201 (2002).

[31] P. S. Barbeau, J. I. Collar, and O. Tench, J. Cosmol. Astropart. Phys. **2007**, 009 (2007).

[32] S. I. Alvis *et al.* (Majorana Collaboration), Phys. Rev. C **99**, 065501 (2019).

[33] N. Abgrall *et al.*, Nucl. Instrum. Methods Phys. Res. A **828**, 22 (2016).

[34] P. Barton, P. Luke, M. Amman, Y. Chan, J. Detwiler, J. Loach, R. Martin, A. Poon, C. Tindall, and K. Vetter, in *Proceedings of the 2004 IEEE Nuclear Science Symposium and Medical Imaging Conference (NSS/MIC2011)*, *IEEE Nuclear Science Symposium Conference Record* (IEEE, Piscataway, NJ, 2011), pp. 1976–1979.

[35] W. Bugg, Y. Efremenko, and S. Vasilyev, Nucl. Instrum. Methods Phys. Res. A **758**, 91 (2014).

[36] K. Vetter, A. Kuhn, I. Lee, R. Clark, M. Cromaz, M. Deleplanque, R. Diamond, P. Fallon, G. Lane, A. Macchiavelli, M. Maier, F. Stephens, C. Svensson, and H. Yaver, Nucl. Instrum. Methods Phys. Res. A **452**, 105 (2000).

[37] J. Anderson, R. Brito, D. Doering, T. Hayden, B. Holmes, J. Joseph, H. Yaver, and S. Zimmermann, IEEE Trans. Nucl. Sci. **56**, 258 (2009).

[38] N. Abgrall *et al.* (Majorana Collaboration), arXiv:2003.04128 (2020).

[39] B. Singh, Nucl. Data Sheets **74**, 63 (1995).

[40] M. Boswell, Y. Chan, J. A. Detwiler, P. Finnerty, R. Henning, V. M. Gehman, R. A. Johnson, D. V. Jordan, K. Kazkaz, M. Knapp, K. Kroninger, D. Lenz, L. Leviner, J. Liu, X. Liu, S. MacMullin, M. G. Marino, A. Mokhtarani, L. Pandola, A. G. Schubert, J. Schubert, C. Tomei, and O. Volynets, IEEE Trans. Nucl. Sci. **58**, 1212 (2011).

[41] S. Agostinelli *et al.* (Geant4 Collaboration), Nucl. Instrum. Methods Phys. Res. A **506**, 250 (2003).

[42] O. A. Ponkratenko, V. I. Tretyak, and Y. G. Zdesenko, Phys. At. Nucl. **63**, 1282 (2000).

[43] C. E. Aalseth *et al.* (Majorana Collaboration), Phys. Rev. Lett. **120**, 132502 (2018).

[44] M. Buuck, A radiogenic background model for the MAJORANA EEMONSTRATOR, Ph.D. thesis, University of Washington, 2019.

[45] H. Akaike, IEEE Trans. Autom. Control **19**, 716 (1974).

[46] I. S. Guinn *et al.* (Majorana Collaboration), J. Phys.: Conf. Ser. **1468**, 012115 (2020).

[47] W. A. Rolke, A. M. López, and J. Conrad, Nucl. Instrum. Methods Phys. Res. A **551**, 493 (2005).

[48] A. Morales, J. Morales, R. Núñez-Lagos, J. Puimedón, J. Villar, and A. Larrea, Nuovo Cimento A **100**, 525 (2008).

[49] B. Maier (Heidelberg-Moscow Collaboration), Nucl. Phys. B, Proc. Suppl. **35**, 358 (1994).

[50] A. S. Barabash, A. V. Derbin, L. A. Popeko, and V. I. Umatov, Z. Phys. A **352**, 231 (1995).

[51] E. A. Coello Pérez, J. Menéndez, and A. Schwenk, Phys. Rev. C **98**, 045501 (2018).

[52] J. Barea, J. Kotila, and F. Iachello, Phys. Rev. C **91**, 034304 (2015).

[53] J. Toivanen and J. Suhonen, Phys. Rev. C **55**, 2314 (1997).

[54] J. Schwieger, F. Šimkovic, A. Faessler, and W. A. Kamiński, Phys. Rev. C **57**, 1738 (1998).

[55] C. M. Raduta and A. A. Raduta, Phys. Rev. C **76**, 044306 (2007).

[56] S. Unlu, Chin. Phys. Lett. **31**, 042101 (2014).

[57] J. Hyvärinen and J. Suhonen, Phys. Rev. C **93**, 064306 (2016).

[58] J. Menéndez, A. Poves, E. Caurier, and F. Nowacki, Nucl. Phys. A **818**, 139 (2009).